Astron. Astrophys. 350, 917–927 (1999)

ASTRONOMY AND ASTROPHYSICS

The physical properties of the HH 30 jet from HST and ground–based data

Francesca Bacciotti[1,2], **Jochen Eislöffel**[3], **and Thomas P. Ray**[1]

[1] School of Cosmic Physics, Dublin Institute for Advanced Studies, 5 Merrion Square, Dublin 2, Ireland (fran,tr@cp.dias.ie)
[2] Osservatorio Astrofisico di Arcetri, Largo E. Fermi 5, 50125 Firenze, Italy
[3] Thüringer Landessternwarte Tautenburg, Sternwarte 5, 07778 Tautenburg, Germany (jochen@tls-tautenburg.de)

Received 12 April 1999 / Accepted 4 August 1999

Abstract. We investigate the physical properties of the HH 30 jet by applying the spectroscopic diagnostic technique described in Bacciotti & Eislöffel (1999) to ground-based spectra and Hubble Space Telescope (HST) calibrated emission-line images. We derive the variation along the beam of the ionization fraction $x_{\rm e}$, of the total hydrogen density $n_{\rm H}$ and of the average excitation temperature $T_{\rm e}$, with a spatial sampling of 0.″1 to 0.″6 (depending on the dataset used) near the source of the flow and of 1.″8 further out. In the jet $x_{\rm e}$ rapidly rises from 0.065 at 0.″2 to 0.1 at 0.″4, and then slowly *increases* up to 0.140 within 2″ from the source. From 2.″4 to 12.″5, $x_{\rm e}$ decreases very slowly down to a value of 0.04. The slow recombination in the outermost collimated part is consistent with a flow opening angle of about 2°. At the beginning of the jet $n_{\rm H}$ is at least $\sim 10^5$ cm^{-3}, but it decreases to 5 10^4 cm^{-3} within the first arcsecond and then slowly falls to 10^4 cm^{-3} at large distance from the source. On average $T_{\rm e}$ decreases from $\sim$ 2 10^4 K to 10^4 K within the first arcsecond of the jet, then it slowly decays to 6000–7000 K. In the faint counter-jet, which appears to be substantially more excited than the jet, $x_{\rm e}$ rises from 0.07 up to 0.35 at 2–3″ from the source, $n_{\rm H}$ decreases from about 8 10^4 cm^{-3} to a few 10^3 cm^{-3}, while $T_{\rm e}$ is scattered around 1.2–1.3 10^4 K. A comparison between the observed and calculated line fluxes shows that *the filling factor is of order unity in this flow*. The emission-weighted jet width calculated with the parameters that we derive is in good agreement with the observed FWHM; we find, however, that the jet radius apparently goes to zero at the source location, defining an initial *full* opening angle of about 10°. The intensity peaks, i.e. the knots, are clearly correlated with local temperature maxima. The ionization fraction and the electron and total densities do not show any evident increase at the same positions, although we cannot exclude the presence of small-scale variations, because of the lower spatial resolution with which these quantities have been derived. Alternatively, the lack of large density enhancements at the locations corresponding to the knots may be due to the presence of a substantial magnetic field in the body of the jet. Anyway, the absence of evident bow-shaped features suggests that in this jet it is more likely that the chain of bright spots traces travelling plasma instabilities, rather than a series of internal working surfaces. Along the jet the mass-loss rate is quite moderate: assuming an average flow speed of 200 km s^{-1}, and adopting as our jet diameter the emission-weighted jet width, we find $\dot{M} \sim 1.7\ 10^{-9}$ M$_\odot$ yr^{-1} and correspondingly $\dot{P} \sim 3.5\ 10^{-7}$ M$_\odot$ yr^{-1} km s^{-1}. In the counter-jet, in contrast, $\dot{M}$ ($\dot{P}$) decreases from about 1.8 10^{-9} M$_\odot$ yr^{-1} (3.6 10^{-7} M$_\odot$ yr^{-1} km s^{-1}) at 0.″6 from the source to about 9.3 10^{-10} M$_\odot$ yr^{-1} (1.9 10^{-7} M$_\odot$ yr^{-1} km s^{-1}) further out.

Key words: ISM: kinematics and dynamics – ISM: jets and outflows – stars: formation – line: formation

1. Introduction

Although the existence of jets from young stars has been known for many years now (see, for example, Ray 1996), their origin remains obscure. Both magneto-hydrodynamic (e.g., Camezind 1990; Shu et al. 1995; Ferreira & Pelletier 1995, Ouyed & Pudritz 1997) and hydrodynamic (e.g., Mellema & Frank 1997) models have been proposed for their generation although to date no definitive observational studies have been carried out to discriminate between these scenarios. If we are to understand how jets arise, then clearly we have to study the 'central engine' itself. Basic principles would suggest that this has a scale of a few stellar radii, i.e. approximately 10^{12} cm, which would require a spatial resolution of 0.5 milliarcseconds for the nearest star forming regions (i.e. at D = 140 pc). This is beyond the capabilities of current instrumentation although planned interferometers, such as the VLTI, should start to approach this goal (Eislöffel & Dougados 1997). In the interim period, we can probe jets close to their source for clues to their origin with a resolution of a few tens of AU using HST. In many cases such studies are difficult because either the source and its surroundings are optically obscure or it is associated with a bright reflection nebula that makes observations of its immediate environment extremely difficult. As it turns out, neither of these problems are very important in the case of Herbig-Haro (HH) 30.

Send offprint requests to: F. Bacciotti

HH 30, in the nearby Taurus-Auriga Cloud, lies at a distance of approximately 140 pc (Kenyon et al. 1994). It was amongst the earliest HH jets to be discovered by Mundt & Fried (1983) who found it to be bipolar with a bright knotty jet, and a clearly extincted counter-jet, emanating from a reflection nebula. Further studies (Mundt et al. 1990, hereinafter MRBRS90; Graham & Heyer 1990; López et al. 1995) showed the flow to be much more extensive than previously thought and that emission associated with the jet and the counter-jet could be traced up to several arcminutes from the source. Rather interestingly the flow was found to wiggle from side to side perhaps as a result of precession or instabilities (see MRBRS90). Spectroscopic studies showed that both the jet and the counter-jet of HH 30 have similar low radial velocities implying that this outflow must be virtually in the plane of the sky (Cohen & Jones 1987; MRBRS90; Raga et al. 1997). Imaging studies with the Wide Field Planetary Camera 2 (WFPC2) on board the HST (Ray et al. 1996; Burrows et al. 1996) found the reflection nebula at the source to consist of two cusp-like structures delineated by a dark region that is almost certainly an edge-on accretion disk (Burrows et al. 1996). Both the jet and the counter-jet were seen to contain a lot more knots than could be resolved from ground-based studies and it was possible to trace the flow to within 0.″2 from the optically invisible source.

We are thus in a sense fortunate that the flared disk in this system acts as a natural 'occulting bar' and hence the HH 30 flow is ideal if we wish to study conditions as close as possible to the region where the jets are generated. With this idea in mind, we have re-analysed existing HST Archive data of the HH 30 flow, coupled with complimentary ground-based data, to perform the first high spatial resolution investigation of the physical properties of its gas using the spectroscopic diagnostic technique described in detail by Bacciotti & Eislöffel (1999, hereinafter BE99). This technique allows one to derive from the ratios of the most commonly observed forbidden lines (i.e. [SII]$\lambda6716+\lambda6731$/[OI]$\lambda6300$, and [OI]$\lambda6300$/[NII]$\lambda6548+\lambda6583$) the ionization fraction $x_{\rm e} = n_{\rm e}/n_{\rm H}$, the total hydrogen density $n_{\rm H}$ and the average excitation temperature $T_{\rm e}$ of the emission region. These parameters are of fundamental importance for any theory of jet formation and evolution as the trends observed in the flows can provide useful constraints for the construction of realistic models of how they are generated in the first place.

After describing details of both the HST and ground-based data used in our analysis in Sect. 2, our results are presented in Sect. 3 and are discussed in Sect. 4.

2. Observational details

The data analysed in this paper consist of a number of CCD images obtained with the Wide Field Planetary Camera 2 (WFPC2) aboard the Hubble Space Telescope (HST), and of two long-slit spectra of the HH 30 jet taken from the ground.

The HST images were part of a study of the HL Tauri region, made in March 1995 (Ray et al. 1996). They were taken with [SII]$\lambda\lambda$6716,6731 (F673N), Hα (F656N), [OI]$\lambda6300$ (F631N) filters, along with a continuum medium bandpass filter in a nearby spectral region (F547M). Total on source integration times were 3×900 s, 2×1800 s, 2×900 s and 2×500 s, respectively, where the first number indicates the number of exposures, which were split to facilitate the removal of cosmic ray hits. The HH 30 jet was positioned on the WF2 CCD of the f/12.9 WFPC2. WF2 has a pixel size of 0.″1 and thus undersamples the HST point spread function (the corrected optics of the WFPC2 gives an Airy disk diameter of 0.″12 at $\lambda = 555$ nm). The images have been calibrated photometrically, using the standard tools available for HST data reduction (for details, see Burrows 1995).

In order to apply the technique to filtered images, a number of operations are necessary. We analysed at each position physical conditions averaged in the transverse direction to the flow, in order to facilitate using the ground-based data (see Sect. 3.1) and the comparison with conditions predicted by theoretical models. Thus, at each position along the flow axis (P.A. = 30°), we considered the light coming from seven pixels (corresponding to 0.″7) covering the jet/counter-jet width. The HH 30 reflection nebula had to be subtracted with the aid of the medium passband image. A direct subtraction from the narrowband images, however, proved to be somewhat difficult due to the faintness of the jet beyond 3.″5 from the source. Also, the fact that the continuum filter has a passband located in a bluer region of the spectrum (from 5000 to 6000 Å) can imply a different colour gradient along the flow with respect to the continuum transmitted by the narrowband filters; in addition, the continuum image includes a few faint lines generated in the body of the jet. This may translate into an over-subtraction of the continuum.

In order to improve the spectral homogeneity of the subtraction procedure, we used the following method: in the continuum image we measured, for each position d along the axis, the total intensity $I_c(d)$ in a rectangular region covering the jet width and one pixel wide, together with the average intensity $I'_c(d)$ of the regions of the same area to the right and the left of the jet. We then evaluated the ratio $I_c(d)/I'_c(d)$, that gives the contribution of the reflection nebula in the region of the jet, with respect to the nebular emission in the lateral regions. Furthermore, we assumed that the relative contribution of the reflection nebula on and off the jet in the light transmitted by the narrowband filters was described by the same quantity. Thus we used the calculated ratio to estimate, at each position from the source in the narrowband images, the contamination by the reflected continuum starting from the nebular emission measured laterally to the jet. We then subtracted the result from the line plus continuum emission measured on the jet section in each narrowband image and at each position along the flow.

One of the ground-based long-slit spectra was taken in 1988 at the 3.5m telescope on Calar Alto, using the Twin Cassegrain spectrograph (P.A. 30°). A standard analysis of the observed lines has been presented by MRBRS90; as it will be explained below, here we will use the electron density and the ratio of the oxygen and nitrogen red lines presented in that work, which were determined by the authors with 0.″6 spatial sampling. The other long-slit spectrum was taken in February 1987 with the

Boller & Chivens spectrograph at the ESO/MPI 2.2-m telescope on La Silla (Chile). Its spectral resolution is about 1.6 Å/pixel and the spatial resolution 1.″8/pixel, determined by the pixel size. The position angle of the slit was 31°. We used this spectrum, despite its poorer spatial resolution, to investigate conditions in the outer part of the flow (beyond 5″ and -2″ from the source in the jet and the counter-jet respectively), since these regions were only barely detectable in the Calar Alto spectrum and in the HST images. For both spectra the line intensity was integrated over the line width. This provides reliable data as input for our technique, especially for fainter regions of the flow, although it does not allow us to disentangle between different velocity components. Such components are in any case not easily identified here, since the HH 30 flow lies nearly in the plane of the sky.

We emphasize that our diagnostic technique does not require correction for reddening for the relative line intensities, due to the limited wavelength range and the choice of the selected ratios (for a discussion of this point, see BE99). In Sect. 4, however, we will compare photometrically the observed fluxes with the fluxes calculated from our results: in that instance we will make the working hypothesis that the main jet lobe is not affected by dust extinction.

3. Results

In this section we illustrate the results of our diagnostic analysis. The filtered images taken with the HST span about 5 arcseconds of the jet and 2 arcseconds in the counter-jet; thus, using the HST images (in conjunction with the Calar Alto spectrum, see below) we zoom into the portion of the flow closest to the source. Here the spatial sampling is about 0.″1 (0.″6 where Calar Alto data are used, see below). Outside this region we used the ESO spectrum, for which the spatial sampling is much poorer, being only 1.″8.

3.1. The central region

The technique requires as inputs an estimate of the electron density, usually calculated from the [SII]λ6716/[SII]λ6731 ratio, and the values of the ratios [OI]λ6300/[NII]$\lambda 6548 + \lambda 6583$, that is basically dependent only on ionization fraction, and [SII]$\lambda 6716 + \lambda 6731$ /[OI]λ6300, that is much more sensitive to temperature variations (in the following the above ratios will be referred to simply as [OI]/[NII] and [SII]/[OI], respectively).

A direct application of the technique to the set of HST narrowband images is difficult, for the reasons we will now describe. First, because both [SII] lines are transmitted by the F673N filter, it is not possible to derive the electron density from the HST data at 0.″1 resolution. Second, we lack an image taken with a narrowband filter in the [NII] lines, that is essential for the determination of the ionization fraction (the Hα filter excludes almost totally the contribution of the nearby [NII] lines, see Burrows 1995). Lastly, as described in detail in BE99, the Hα image is of no use for our diagnostic technique, due to the fact that Hα emission comes from regions with physical characteristics that are not identical to those producing the forbidden lines.

In order to partly overcome these difficulties, one is forced to use the information contained in the ground-based data, at least for the electron density and the [NII] emission along the jet. Thus, as our estimate of $n_{\rm e}$ we used a fit for the electron density values calculated from the Calar Alto spectrum in MRBRS90. Note that this spectrum was taken 7 years earlier than the HST images. Thus, if the knots are associated with clumps of matter with higher density than the average flow, the fact that such knots have moved rapidly in the elapsed time (MRBRS90, Burrows et al. 1996) may in principle lead to mis-diagnoses of the physical quantities. We stress, however, that the electron density profile determined with that spectrum did not seem to be correlated with the co-eval pattern of knots (see Fig. 20 of MRBRS90). Therefore we concluded that the density determined by the ratio of the [SII] lines, is the one corresponding to the underlying flow, and we assumed that this has not changed dramatically within the timespan of our observations. We also used the results of MRBRS90 to determine the ratio between the oxygen and nitrogen lines to be associated with the [SII]/[OI] ratio derived from the HST images. As for the electron density, the [OI]/[NII] ratio determined by MRBRS90 did not show any correlation with the co-eval positions of the knots. Thus we assumed that the values of the [OI]/[NII] ratio have not changed a lot in the time elapsed between the two observations, and we calculated a fit of the ratio values as determined from the ground-based spectrum. Then,if $[\mathrm{OI}]_{\mathrm{HST}}(d)$ is the intensity of the [OI]λ6300 in the HST image integrated across the beam, the corresponding [NII] intensity in a hypothetical [NII] image taken with HST would be $[\mathrm{NII}]_{\mathrm{HST}}(d) = [\mathrm{NII}]_{\mathrm{CA}}(d)/[\mathrm{OI}]_{\mathrm{CA}}(d)\cdot[\mathrm{OI}]_{\mathrm{HST}}(d)$, where $[\mathrm{NII}]_{\mathrm{CA}}(d)$ /$[\mathrm{OI}]_{\mathrm{CA}}(d)$ is the value of the fit of the ratio derived from the Calar Alto spectrum associated with position d in the HST data.

Of the 7″ examined, the application of the technique was found to give accurate results only in the first 4″ of the jet, while in the counter-jet and in the terminal portion of the jet the results turn out to be 'noisy', because of the faintness of the lines in these regions. Indeed, in the counter-jet only a few positions corresponding to the centres of the first two bright knots provided reliable readings. In the jet, in contrast, we were even able to investigate the inter-knot regions.

The results we obtained for the central region are presented in Fig. 1. Panel *a* is a contour plot of a HST [SII] image of the jet and the counter-jet, after subtraction of the reflection nebula. Panel *b* shows the intensity tracings of the emission lines integrated over seven pixels across the beam, all normalized to the [SII] peak. The [NII] intensity tracing derives from a ground-based spectrum, as described above. Note that within 0.″2–0.″9 from the source the [OI]λ6300 line is stronger than any other line, including the sum of the two sulphur lines. It is also evident that Hα is much more intense than the forbidden lines in the counter jet, while its contribution is smaller in the main jet. This is consistent with the results of our diagnostic technique (see below), that indicate the counter-jet to be of higher excitation than the jet. Note, however, that the Hα emission of the initial

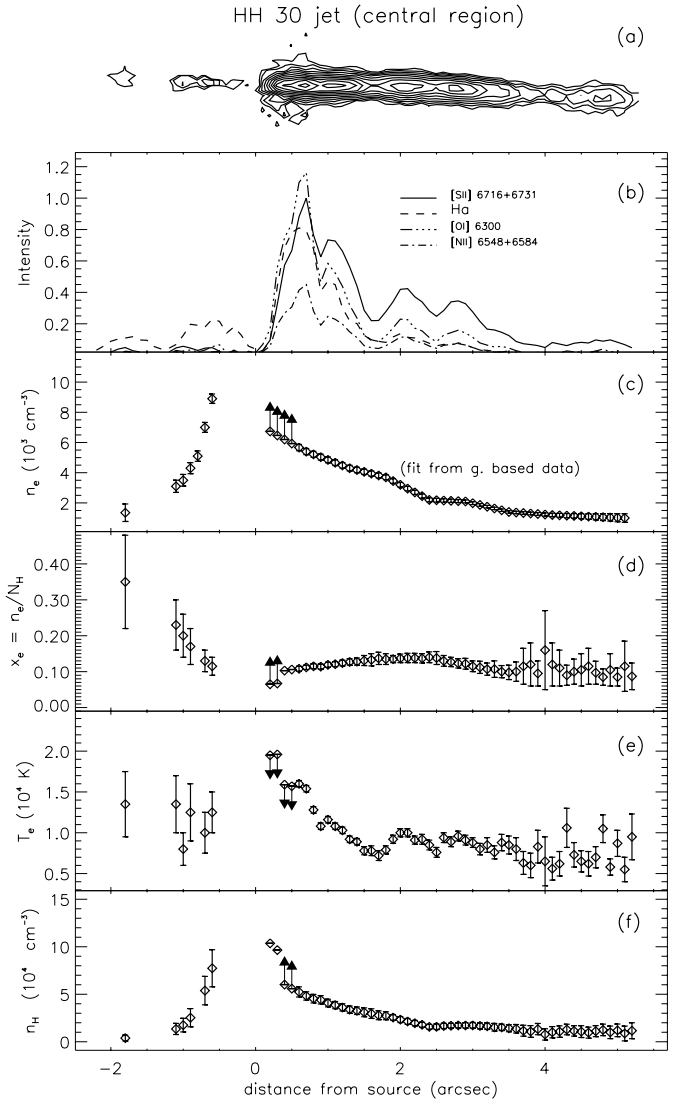

Fig. 1a–f. Physical conditions in the central region of the HH 30 jet. **a** Contour plot of the [SII] HST image. **b** Intensity tracings in the various lines integrated across the jet beam and normalized to the [SII] peak - the [NII] emission profile derives from the ground-based observations, while the other lines were measured on HST images (see text). **c** Electron density calculated as a fit of the ground-based results in MRBRS90. **d** Hydrogen ionization fraction $x_{\rm e}$. **e** Average excitation temperature of the forbidden line emission region. **f** Total hydrogen density $n_{\rm H} = n_{\rm e}/x_{\rm e}$. The arrows indicate limiting values (see text).

part of the jet could still be highly contaminated by the Hα emission coming from the source: this problem is not completely ruled out by the subtraction of the reflection nebula that we performed on the images.

The electron density, as derived from the fit described above, is illustrated in panel *c*. We stress that the values close to the source are lower limits (as denoted by the arrows), since the [SII] lines are quenched in these positions. This is clear from the fact that the [SII]/[OI] ratio is quite low in the region close to the source, while it is higher in the more distant parts of the jet (see Fig. 2, panel *a*). This effect, already observed for HH 30 by MRBRS90 in their spectrum, seems to be common amongst others HH flows in the proximity of their source (Hartigan et al. 1995a; Hirth et al. 1997). Quenching, in turn, can alter the results derived from the diagnostic, since collisional deexcitation is included in the code. As an example, we have estimated the effects of an assumed 30% increase in the electron density in the first 0.″5 from the source (four positions). In this case, the temperature turns out to be lower by about 12% in all the examined positions. In contrast, the ionization fraction is higher by 35% in the first two positions, while at 0.″4 and 0.″5 it increases only by 3–4%, that is less than the measurement error. This peculiar behaviour for $x_{\rm e}$ is due to the fact that here the strips of the diagnostic diagram cross in a region where the [OI]/[NII] ratio changes its slope (see BE99). As a consequence, the total density turns out to be practically unaffected in the first two positions, while it increases by 25–27% at 0.″4 and 0.″5. The variations in the various quantities estimated above are indicated by arrows in panels *d – f*.

In panel *d* we illustrate the results for the ionization fraction. The analysis shows that at the beginning of both the main flow and the counter-jet the ionization fraction *increases*. In the jet it grows rapidly from 0.065 at 0.″2 to 0.1 at 0.″4; from this point up to about 2.″4 $x_{\rm e}$ then increases monotonically to 0.140, and subsequently declines again to 0.1 at position 3.″5. After this point the results begin to be noisy; however, the average $x_{\rm e}$ seems to decrease further to about 0.08 in the last position examined using the HST data, at 5.″2. In the first knot of the counter-jet, the ionization fraction appears to rise from about 0.07 close to the source up to 0.23 at -1.″1. In the second knot only one position has a readable result, though affected by big uncertainty: here $x_{\rm e}$ is even higher, reaching 0.35. The relatively high ionization of the counter jet is confirmed also by the analysis of the ESO spectrum (see Sect. 3.2).

The behaviour of the average excitation temperature revealed from the high resolution HST images is illustrated in panel *e*. Close to the source ($\leq 1''$), the flow presents high temperatures (up to $\sim 2\ 10^4$ K, at 0.″2 in the jet and about $1.3\ 10^4$ K, in the counter-jet). $T_{\rm e}$ decreases then rapidly to 10^4 K within the first arcsecond of the jet, and then it decays more slowly to reach values as low as 6000–7000 K toward $5''$. In the second knot of the counter-jet, in contrast, the gas is apparently as hot as closer to the source.

The trends revealed for the ionization fraction and the temperature are of great interest concerning the identification of the excitation and acceleration mechanisms. A discussion of this point will be given in the next section.

Finally, panel *f* illustrates the total hydrogen density as derived from the ratio $n_{\rm e}/x_{\rm e}$. This quantity is extremely high at the beginning of the main jet, being at least 10^5 cm^{-3} in the first two positions. It then decreases to $5\ 10^4$ cm^{-3} within one arcsecond and then steadily falling to 10^4 cm^{-3} at $5''$. In the counter-jet the total density decreases from about $8\ 10^4$ cm^{-3} to 10^4 cm^{-3} in the first knot, and it is apparently only a few 10^3 cm^{-3} in the second knot. We remark that also if in the first positions close to the source the values we provide for the total density are actually lower limits, the HH 30 jet is the densest we

have examined so far. A valuable check to the derived values for the density may come from an estimate of the filling factor in the jet. We will discuss this point in detail in the next section.

3.2. The outermost parts

In the following we illustrate the results for the distant parts of both the jet and the counter-jet, as derived from the analysis of the spectrum taken at La Silla. The values obtained for the physical quantities are presented in Fig. 2. The inlay central part of the figure is a sketch of the results illustrated in Sect. 3.1 (without errors).

Panels *a* and *b* show the input values of the [SII]/[OI] and the [OI]/[NII] ratios, respectively. In panel *c* we present the values of the electron density $n_{\rm e}$ as derived from the ratio of the [SII] lines. In the counter-jet $n_{\rm e}$ stays constant at about $\sim 1600\,{\rm cm}^{-3}$, while in the main jet the electron density follows the decay initiated in the central part, decreasing from about $1100\,{\rm cm}^{-3}$ in position 7.″1 to about $370\,{\rm cm}^{-3}$ at 10.″6 from the source. Then it rises again up to $640\,{\rm cm}^{-3}$ in the last position examined. The continous line superimposed to the data is a theoretical recombination curve (see below).

The ionization fraction values derived for the outermost parts are illustrated in panel *d*. There is marginal evidence that $x_{\rm e}$ decreases in the section from 7.″1 to the last position examined, at 12.″5. The recombination curve superimposed to the plot is calculated with a simple model in which the gas is assumed to flow in a series of nested cones (see BE99 for details). As input parameters one has to specify the jet radius $r_{\rm j_0}$ at the first position in which the ionization begins to fall; the distance of the object, which we take to be 140 pc; the inclination angle of the beam with respect to the plane of the sky, here assumed to be zero degrees, and an average value of the jet speed $\bar{v}_{\rm j}$. As jet radius we take 0.″09 at d =2.″5 (see next section for the derivation of this estimate). The jet velocity is poorly known. MRBRS90 estimated the average tangential velocity of the knots to be about $170\,{\rm km\,s}^{-1}$ in the jet, in agreement with more recent determinations by Burrows et al. (1996), who find that the knot speed ranges between 55 and $260\,{\rm km\,s}^{-1}$. Since the jet lies nearly in the plane of the sky, and if the knots represent a material concentration moving away from the source, the tangential velocity will be the actual bulk velocity of the flow; the knots, however, could also trace a moving pattern of instabilities in a flow of different speed (see Sect. 4). In this case, the actual flow velocity could be determined only from the Doppler shift of the lines, combined with an estimate of the inclination angle of the jet. Given the peculiar inclination of this flow, however, determinations of this kind are extremely difficult: for example, MRBRS90 and, more recently, Raga et al. (1997) derive similar *positive* values of the heliocentric radial velocity ($\sim 20\,{\rm km\,s}^{-1}$) in *both* the jet and the counter-jet. For this reasons we will simply assume that the velocity of the matter is $200\,{\rm km\,s}^{-1}$; similar velocities, that are of the order of the escape velocity from the stellar surface, have been found for other outflows from young stars. Both the recombination curves superimposed to the ionization fraction and the electron density profiles are calculated with the previous set of parameters, and with a *full* opening angle in the outer part of the flow of only 2°: a justification for this choice will be given in the next section. Finally, the results for the counter-jet confirm that there the ionization is substantial, being 0.35 at -3.″6 and 0.23 at the last position examined.

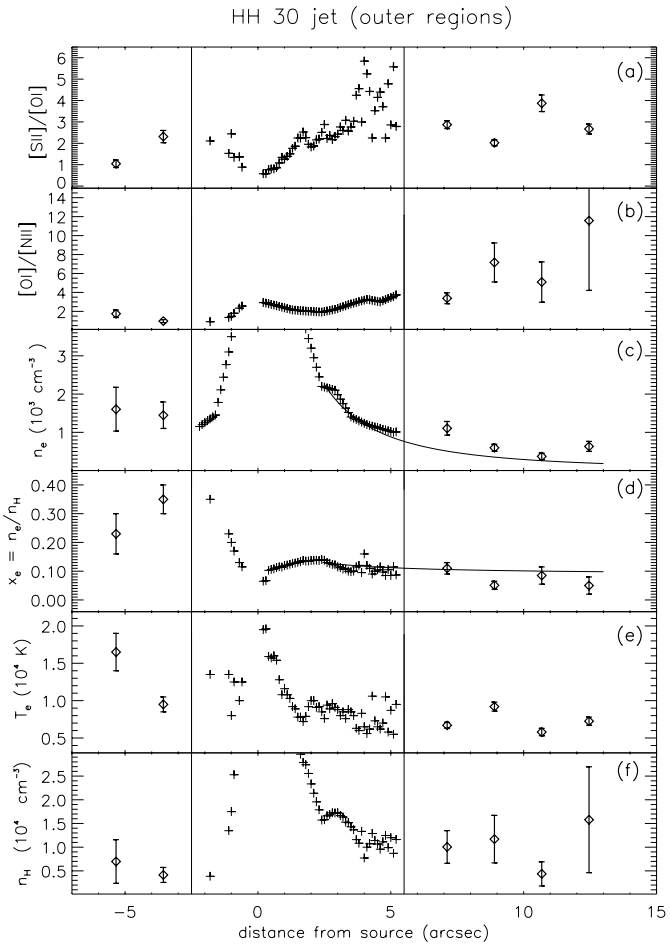

Fig. 2a–f. Physical conditions in the outermost parts of the HH 30 jet and counter-jet, as derived from the ground-based spectrum. **a** [SII]/[OI] line ratio. **b** [OI]/[NII] ratio. **c** Electron density derived from the [SII] line ratio and superimposed recombination curve (see text). **d** Hydrogen ionization fraction $x_{\rm e}$ plus recombination curve. **e** Average excitation temperature of the forbidden line emission region. **f** Total hydrogen density $n_{\rm H} = n_{\rm e}/x_{\rm e}$. The central inlay part is a sketch of the results illustrated in Sect. 3.1

The average excitation temperature of the emission region of the forbidden lines is shown in panel *e*. According to the ground-based analysis the temperature is always lower than 10^4 K in the outer part of the main jet: it is only 6700 K at position 5.″3, then it rises to about 9200 K at position 8.″9 and subsequently falls to about 7000 K at the end of the examined region. In the counter-jet, on the contrary, it increases from $\sim$ 7000 K at 3.″6 to 16500 K at -5.″3. The results for the last positions examined in both flows, however, should be taken with caution due to the faintness of the lines.

Finally, panel *f* presents the behaviour we derive for the total hydrogen density $n_{\rm H} = n_{\rm e}/x_{\rm e}$. The total density is about

10^4 cm^{-3} on average in the outermost part of the jet, while it is as low as 5–6 10^3 cm^{-3} in the outer counter-jet.

4. Discussion

Before discussing our results, it is worthwhile clarifying the meaning of the values we derive from the diagnostic. In BE99 we noted that at the resolution of the spectra investigated there (1.″8 / pixel) the resulting values for $x_{\rm e}$ and $T_{\rm e}$ were averages over a large parcel of gas, possibly including unresolved regions with large variations of the physical quantities, as in the cooling region of a radiative shock. The ionization, however, can still be considered representative of the conditions of the emitting gas as a whole, since in the post-shock cooling layer the ionization rapidly reaches a plateau that is maintained over a large distance (see, e.g., Hartigan et al. 1994); in contrast, $T_{\rm e}$ is only a rough indication of the excitation temperature, since it varies considerably behind the shock. This remark should be taken into account when considering the results derived in Sect. 3.2, since the spectrum with which we investigated the outer regions of the flow has the same spatial resolution as those analyzed in BE99. The situation, however, may be different for the data from HST, since the spatial sampling is 0.″1 (corresponding to 2.1 10^{14} cm at the distance of Taurus-Auriga). The cooling region of a plane-parallel standing shock may vary between 10^{13} cm and 10^{15} cm depending on the shock strength and the pre-shock density; it should be considered, however, that several effects may stretch these distances by a factor between 10 and 100 in a realistic situation. These are, for example, the obliqueness of the front with respect to the flow, the divergence of the flow surfaces, the relative velocity between the front and the underlying plasma, the presence of a substantial component of the magnetic field parallel to the shock front. Thus, for a nearby flow like HH 30, values derived using a diagnostic technique from HST data could, in principle, be considered a good representation of a real local value. In the present case, however, we have been forced to use fits of the ground-based [SII]λ6716/[SII]λ6731 and [OI]/[NII] ratios, that were determined by MRBRS90 with 0.″6 spatial sampling; thus the small scale variations of the electron density and the ionization fraction (and hence, of the total density) are actually smeared over that length. We note, anyway, that the HST emission profiles show noticeable variations over distances larger than that, thus corresponding variations in the ionization and the densities should be detected if present. On the other hand, the temperature is practically fixed by the value of the [SII]/[OI] ratio, which was derived using only the HST images. We also recall that having integrated the emission of the jet across the beam, we do not investigate in this work the transverse trends of the physical parameters.

4.1. Variation of the quantities along the beam

The application of our technique to both spectral data and images of the HH 30 jet has revealed that this flow is weakly ionized, with the ionization fraction less than 0.15 in most part of the jet, reaching 0.35 only in the counter-jet far from the source. Partial ionization appears to be a common characteristic of Herbig-Haro jets. In BE99 we examined long-slit spectra of the jets HH 34, HH 46/47, HH 24E/C/G, the HL Tau jet and HH 228 (Th 28 jet). There we found that $x_{\rm e}$ generally ranges between 0.02 and 0.4, being higher for lighter and more excited jets.

Contrary to what is observed in HH 30, however, in most of the above mentioned jets the ionization fraction was found to *decrease* along the flow, following well-defined recombination curves. In some jets a number of re-ionization events were observed; also in that case, the decay in $x_{\rm e}$ is always located downstream of the ionization jump. The only cases where the ionization was found to increase moving away from the source are the HL Tau jet and the 'beam' section of the Th 28 flow. The case of the HL Tau jet, however, is not directly comparable with the present one, since the bright section of the jet lies quite far away ($\sim 16''$) from the most probable source. In contrast, Th 28 presents remarkable similarities with HH 30. In TH 28, the jet can be traced all the way to the source, and the ionization fraction is shown to increase substantially (from 0.07 to 0.6) in the first portion of the jet, and subsequently is scattered around a constant value. Moreover, both the densities and the temperature are observed to decrease along the jet, as in HH 30.

These facts lead one to suspect that the increase of the ionization in the first few arcseconds from the source may be a trace of the mechanisms operating in that region, and all jets might show the same features when observed close to the source and at high resolution. Pronounced gradients in the gas parameters on sub-arcsecond scales from the source have recently been derived for other optical outflows (Hirth et al. 1997, Lavalley et al. 1997). On the other hand, for those jets for which the source is deeply embedded in the parent cloud, or that lie too far away for the central regions to be observed at sufficient resolution, only the subsequent recombination section would be detected, as we found in our analysis in BE99. Indeed, a recombination decay in both the ionization fraction and the electron density is recognizable also in the outermost part of the HH 30 jet, starting from 2.″5 from the source (see Fig. 2).

The ionization in the beam may be produced in the first place close to the source, for example as a consequence of ambipolar diffusion heating in a magnetized flow (Safier 1993a, 1993b) or by one or more oblique shocks at the base of the jet (e.g., Ouyed & Pudritz 1993, Hartigan et al. 1995a, Mellema & Frank 1997). In the case of the HH 30 jet this hypothesis is substantiated by the observations of Burrows et al. (1996), who find that the observed average integrated brightness per unit length varies as d^{-2}, where d is the distance from the star. The authors argue that the recombination time scale is long with respect to the travel time through the bright jet section (160 and 20 years respectively), so if the ionization is produced close to the source and the gas expands freely in the transverse direction (as indicated by the estimates of the jet radius (see Sect. 4.2)), the brightness variation is understandable and no additional energy input is necessary. Indeed, at a first glance the behaviour of $x_{\rm e}$ and $T_{\rm e}$ with distance from the source is reminiscent of the one prescribed for a post-shock cooling region with the front located

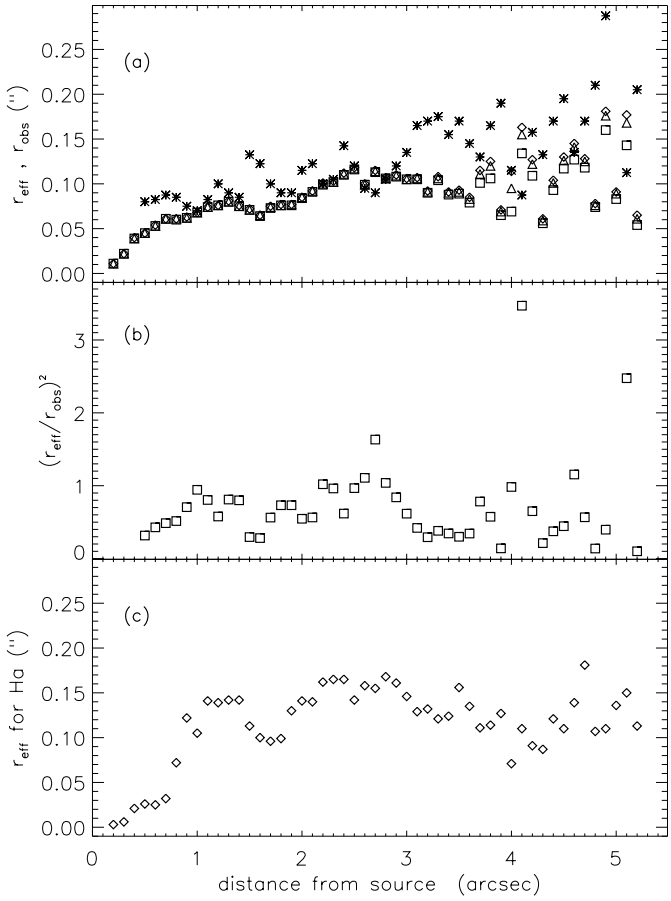

Fig. 3a–c. Filling factor in the central region of the HH30 jet. **a** Emission-weighted effective jet radii ($r_{\rm eff}$) calculated for the [SII], [OI] and [NII] line emissions ('diamonds', 'triangles' and 'squares' respectively); the 'asterisks' illustrate the deconvolved FWHM/2 $\equiv r_{\rm obs}$ from Burrows et al. (1996). **b** Ratio between the square of the calculated effective radius in [SII] and the square of the deconvolved FWHM/2, as a measure of the filling factor. **c** Indicative determination of the emission-weighted effective radius in Hα.

within the first tenth of arcsecond. In fact, the ionization fraction derived from our diagnostic is consistent with the plateau region of the x_e profile provided by simple shock models (see, e.g., Hartigan et al., 1994). At the same time, the temperature rapidly decreases from 2.3 10^4 K to 10^4 K in less than one arcsecond, and then slowly falls to 5000 K at the end of the flow. Also if the apparent similarities are tempting, however, only a refined radiative shock model calculated with input parameters consistent with our results could assess if this scenario is correct.

4.2. Filling factor

As mentioned in the previous section, a valuable check to the derived values of the densities is the determination of the filling factor of the flow, that is the fraction of the volume of the jet channel occupied by the emitting material.

To estimate the filling factor, we compared the flux observed in the calibrated HST narrowband images with the flux calculated from the parameters obtained using our diagnostic. Since we integrated the emission across the jet beam (see Sect. 2), this reduces to a comparison of the observed radius $r_{\rm obs}$ as determined from the Full Width Half Maximum (FWHM) of the transverse emission profile, and the emission-weighted 'effective' jet radius $r_{\rm eff}$, defined as the radius of the channel which, uniformly filled with matter at the corresponding $n_{\rm e}$, $x_{\rm e}$ and $T_{\rm e}$, would produce the observed radiation flux in the considered line.

We only performed this test for the main jet, for which we made the working hypothesis that it is not obscured by dust (see Sect. 4.5). We also assumed that the gas is optically thin in the lines considered, that the jet section is circular and that the jet axis is in the plane of the sky.

The result of our analysis is shown in Fig. 3. In panel *a* the 'asterisk' symbols are one half the deconvolved FWHM adapted from Fig. 5 of Burrows et al. 1996, while the 'diamond', 'triangle' and 'square' symbols are the values of the emission-weighted effective radius calculated by us in the [SII], [OI] and [NII] lines respectively. The agreement between the observed and effective radii turns out to be fairly good. There is little evidence for an anticorrelation between the observed radius and the emission peaks, while we do not see any such correlation in the calculated effective radii. We also note that the deconvolved FWHMs of Burrows et al. 1996 are smaller than the raw data by 35% on average (see their Fig. 5).

In panel *b* we give the square of the ratio between the calculated [SII] effective radius and the observed radius: this quantity is a measure of the filling factor. The calculated ratio scatters around an average value of ~ 0.7: this implies that *the filling factor is of order unity*, at least in the first section of the jet. We find no strong evidence for radiative shocks with high compression ratios (in contrast to, for example, Hartigan et al. 1994, 1995b). Note, however, that $(r_{\rm eff}/r_{\rm obs})^2$ slightly increases locally at the position of each emission peak, except for the one at $d = 0.7$.

Our calculations also indicate that while in the collimated portion (beyond about 0.″7) the average *full* opening angle is only 2°, the effective radius goes to zero at the source location, with an initial *full* opening angle of about 10°. It should be pointed out, however, that the density determination in this part of the flow suffers from diagnostic uncertainties (see Sect. 3.1), that in turn may affect our determination of the effective radius. If in the first positions the actual density is higher than that determined by the diagnostic, the derived radius would be smaller. On the other hand, we cannot exclude that the decay of the observed emission at the beginning of the jet is caused by local strong extinction due to circumstellar material, and in this case the effective radius may be larger than that determined.

Finally, we report on a qualitative calculation of the effective radius of the jet for Hα emission (see Fig. 3, panel *c*). This determination, however, has only an indicative character, since, as discussed in BE99, the region of emission of the forbidden lines, for which the diagnostic provides the values of the physical quantities, is not the same as that in which the Hα emission is produced. In the first 0.″7, where the high temperature causes the

Hα collisional contribution to dominate, the effective radius is about one half that determined for the forbidden lines. This may indicate that the subtraction of the reflection nebula is particularly critical in the circumstellar region, where the reflected Hα may be produced either on the stellar surface or in the jet itself. It should be noted, however, that collisional Hα is extremely sensitive to temperature, so that the uncertainty with which $T_{\rm e}$ is determined does not allow us to draw firm conclusions for the first positions from the source. On the contrary, the result obtained for the region beyond $d = 0\farcs7$, where the temperature drops, recombination Hα dominates, and the reflection nebula does not affect the jet emission anymore, gives an interesting indication on the nature of the jet. Here the calculated effective radius is about 1.5 times larger than the radius determined for the forbidden lines. Such an increase of the apparent jet width is not seen in the Hα image. On the other hand, recombination Hα is inversely proportional to temperature, thus this result may indicate that consistent amounts of material, too cold to be observable in the forbidden lines, may be present at the boundaries of the jet. This in turn may affect the determinations of quantities that depend on the total mass content of the flow (see Sect. 4.4).

4.3. On the nature of the knots

The excitation of the chain of bright knots in the beam of a stellar jet is generally attributed to shocks that locally heat the gas. These may be produced by plasma instabilities arising either in the interaction with the surrounding medium or in the evolution of magnetohydrodynamic waves propagating along the internal magnetic field lines (see, e.g., Bodo et al. 1994, Stone et al. 1997, Hardee & Stone 1997, Bacciotti et al. 1997, Ouyed & Pudritz 1997, Micono et al. 1998, Downes & Ray 1999). Alternatively, the internal shocks arise as a consequence of variations in the ejection mechanism, that may consist either in quasi-periodic variations in the outflow velocity or in the pulsed ejection of separate cloudlets (see, e.g., Stone & Norman 1993, Falle & Raga 1993, 1995, Raga & Cantò 1998). In the first case the bright knots represent the pattern of instabilities acting on an underlying continous flow, whereas in the latter case the knots can be resolved either in mini-bow shocks with the bows pointing away from the source, or in a series of clumps of enhanced density with respect to the average.

Indeed, the knots in the HH 30 jet do not show the shape usually associated with mini bow-shocks, and it has been recently proposed that the excitation in the beam may have a different origin (Ray et al. 1996, Burrows et al. 1996). Our analysis, in addition, offers further constraints to the hypotheses concerning the nature of the knots in this jet. In fact, from a cursory inspection of panel *b* of Fig. 1 and panel *a* of Fig. 2, one can notice that the intensity peaks identifying the knots are apparently correlated with local minima of the [SII]/[OI] ratio, which in turn correspond to local temperature peaks (panel *e* of Fig. 1). As we noted in Sect. 4.2,, there is also marginal evidence that the filling factor peaks in the locations corresponding to the bright knots. In contrast, neither the ionization fraction nor the derived jet density show any obvious recurrent feature at the location of the knots (see Fig. 1), although the existence of small scale variations in $n_{\rm e}, x_{\rm e}$ and $n_{\rm H}$ cannot be ruled out, because of the limited spatial resolution of the ground-based spectrum from which these quantities have been derived (see Sect. 3.1 and MRBRS90).

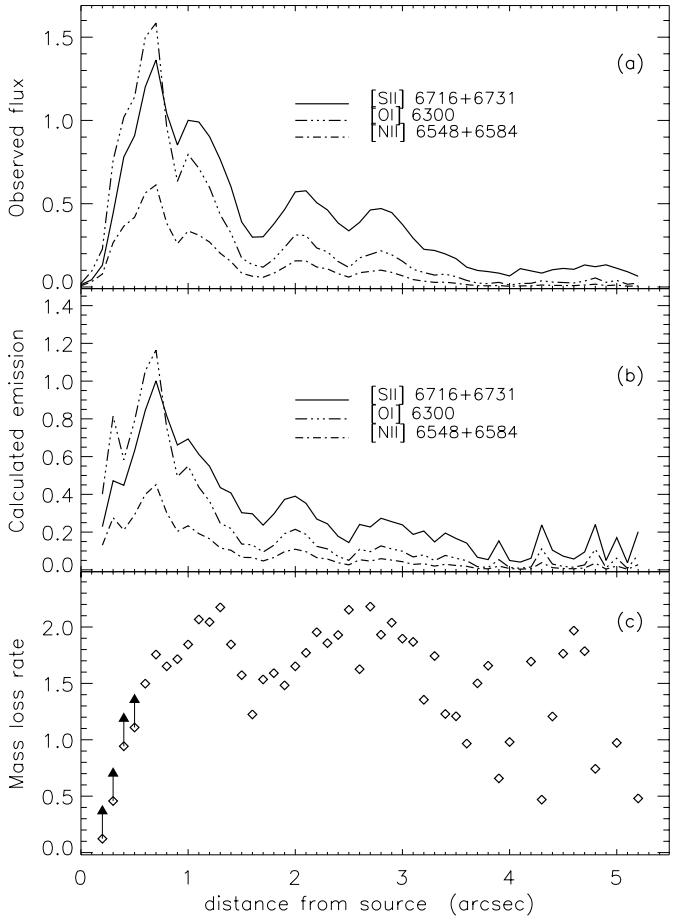

Fig. 4a–c. Emission profiles and mass loss rate along the HH 30 jet. **a** Calibrated intensity tracings observed in the forbidden lines, in units of 10^{-14} erg s^{-1} cm^{-2} arcsec^{-2}. **b** Intensity tracings normalized to the [SII] peak calculated with the physical parameters derived by the diagnostic and a linear fit to the values of the effective radius illustrated in panel *a* of Fig. 3 **c** Mass loss rate in units of 10^{-9} M$_\odot$ yr^{-1} calculated with $v_{\rm j} = 200$ km s^{-1} and the [SII] emission-weighted radius.

We point out, however, that the limited temperature variations we find are sufficient to create the observed pattern of bright spots, even if we calculate the emission using our results for the density and the ionization fraction, and a linear approximation to the jet radius: the intensity tracings derived in this way, illustrated in panel *b* of Fig. 4, are remarkably similar to the observed profiles, shown in panel *a*. We stress that also assuming the presence of a 30% undetected increase in the electron density at the position of the emission peaks, the diagnostic would still provide a peak in the temperature in correspondence with the [SII]/[OI] minima. It might be also interesting to note that recent observations of the L483 jet in the infrared emission lines of H_2 show evidence that the series of peaks and troughs in

the emission profile along the jet is correlated with temperature rather than density variations (Buckle et al. 1999).

In conclusion, we can affirm that the knots in the HH 30 jet are unambigously related to temperature peaks, and that there is marginal evidence for enhancement of the filling factor in the same positions. On the other hand, our data do not allow us to ascertain if simultaneous enhancements of the density and/or the ionization fraction are present in the same locations, although they do not seem to be necessary for the emission profile to be reproduced. This is intriguing, since every model of knot formation among the studies mentioned above prescribes that the density should increase at the position of the bright spots. One way of reducing density enhancements is the presence of a magnetic field in the body of the jet. If an important component of the field lies parallel to the front of the radiative shocks, the post-shock compression can be reduced substantially. For example, Hartigan et al. (1994) estimate that in a plane/parallel shock, with pre-shock density of 10^3 cm^{-3} and shock velocity 40 km s^{-1}, a magnetic field of 300 μG would reduce the compression (defined as the ratio between the pre- and the post-shock densities) from 35 to only 2.5. The reduction of the density increase due to the presence of magnetic fields at the location of developing internal shock fronts is also evident in the simulations of Hartigan & Raymond (1993). We also note that MRBRS90 invoked the presence of a toroidal magnetic field to explain the apparent bending of the HH 30 jet with increasing distance from the source.

In any case, the absence of evident bow-shaped structures seems to suggest that in this jet the chain of bright spots traces a pattern of plasma instabilities rather than a series of internal working surfaces.

4.4. Mass loss and momentum transfer rates

It is interesting to give an estimate for the mass loss and the momentum supply rate associated with the flow. These quantities can be expressed as $\dot{M} \equiv \pi r_{\rm j}^2 \rho v_{\rm j}$ and $\dot{P} = \dot{M} v_{\rm j}$ respectively, where ρ, $r_{\rm j}$ and $v_{\rm j}$ are the total mass density, the jet radius and the flow velocity in each position. Assuming an average jet velocity of 200 km s^{-1} (see Sect. 3.2), a mean molecular weight for neutral atomic gas of 1.24, and a fraction of hydrogen atoms with respect to the total of 0.921 (Allen 1973), panel *c* of Fig. 4 illustrates the mass loss rate derived using the [SII] emission-weighted effective radius and the total hydrogen density in Fig. 1. If exception is made for the first 3–4 positions from the source, $\dot{M}$ is about 1–2 10^{-9} M$_\odot$ yr^{-1} up to large distances in the main jet. The momentum transfer rate is, in turn, $\dot{P} \sim$ 2–4 10^{-6} M$_\odot$ yr^{-1} km s^{-1}. Looking at the data in panel *c* there is marginal evidence for a slight decrease in the average mass loss rate, consistent with the average variation of the density and of the effective radius along the flow. Since we took a constant velocity and the total density has a smooth profile, the oscillations of $\dot{M}$ along the flow reflect the variations in the adopted jet radius (see Fig. 3, panel *a*). The apparent rapid decrease in the mass loss rate toward the source, on the contrary, is not clearly understood. Unless at the present moment we are observing a very peculiar stage of mass ejection, the derived decrease of the mass loss rate probably indicates that the electron and total density are underestimated close to the source. As mentioned in Sect. 3.1, this argument is supported by the observed reduction of the [SII]/[OI] ratio in that region, that suggests quenching of the [SII] lines; on the other hand, the 0.″6 spatial sampling with which $n_{\rm e}$ has been determined in MRBRS90, although sufficient for slow variations to be detected along the beam, may not be enough for an adequate representation of the steep density gradients likely present in the proximity of the source. Alternatively, we may have underestimated the [SII] effective radius in the first positions, if the observed emission is extincted substantially by circumstellar material prior to position $d = 0.''5$ (see Sect. 4.2).

Since the counter-jet is possibly obscured by the parent cloud (see below), we did not attempt any determination of the effective radius here. Nevertheless, an indicative value of the mass loss rate can be calculated assuming as jet diameter the deconvolved FWHM provided in Burrows et al. (1996), and a flow velocity of 200 km s^{-1}. Contrary to the jet, here we derive a steep decay in both $\dot{M}$ and $\dot{P}$ moving away from the source, due to the sudden drop of the density. Here $\dot{M}$ decreases from about 1.8 10^{-9} M$_\odot$ yr^{-1} at 0.″6 from the source to about 9.3 10^{-10} M$_\odot$ yr^{-1} further out. The momentum supply rate follows the same trend. Such a steep drop may indicate that the jet is violently interacting with its surroundings, or, alternatively, that we are looking at a region of strongly non-uniform density. Given the poor accuracy of the results we obtain for the counter-jet, we refrain to draw further conclusions from this evidence.

The derived mass loss rate in the HH 30 jet, although in the range determined by Hartigan et al. (1995a) for a large sample of T Tauri stars showing evidence of simultaneous accretion and ejection, turns out to be quite moderate with respect to those derived in BE99 and Hartigan et al. (1994) for more similar Herbig-Haro jets. The density in HH 30 is high, thus the smallness of the calculated rates appears to be due to the fact that the jet channel is quite narrow. However, the emission-weighted jet radius $r_{\rm eff}$, that we have adopted in our calculations, may not be a good representation of the mass-weighted radius $r_{\rm M}$. We already pointed out in Sect. 4.2 that the comparison amongst the observed and calculated recombination Hα fluxes indicate that the boundary regions of the jet may indeed contain a significant portion of the mass but be too cold to be detected. Thus we may have underestimated both the mass loss and the momentum supply rate by a factor proportional to $(r_{\rm eff}/r_{\rm M})^2$.

Even smaller values than those determined by us were derived for HH 30 by MRBRS90, who estimate $\dot{M} \sim 1.5\ 10^{-10}$ M$_\odot$ yr^{-1} in the jet and $\dot{M} \sim 3\ 10^{-10}$ M$_\odot$ yr^{-1} in the counter-jet. These authors, however, in spite of assuming a jet velocity two times greater than ours and a distance of the object of 160 pc, took as an average value for the electron density in the whole jet the one determined at $5''$ from the source, which is only 700 cm^{-3}. They also assumed complete ionization, and, in addition, they took into account shock compression, that according to their excitation estimates leads to a very low pre-shock density, $N = 65$ cm^{-3}.

4.5. Asymmetries in the two lobes

Our analysis confirms that the counter-jet is substantially more excited than the jet, although it is seen to be much fainter in the images. Indeed, assuming a filling factor for the counter-jet comparable to the one of the main jet (Sect. 4.2), and taking the values of the physical parameters for this region derived by our diagnostic one would derive higher line intensities in the counter-jet. We note that according to the optical wide-field images presented by López et al. 1995 (see their Fig. 1) the counter-jet lies at the border of a large dark region apparently free of stars, that extends to the south/south-east of the flow over an area of at least $4' \times 4'$. This could suggest that the relative faintness of the counter-jet is due to the fact that it propagates into the parent cloud.

Nevertheless, major differences are observed that cannot be explained by extinction effects. Both Ray et al. (1996) and Burrows et al. (1996) noted that the observed FWHM of the counter-jet appears broader at a given distance from the source. We also derive different behaviours for the variations of the physical parameters: the rise and fall of the ionization fraction are much more steep in the counter-jet, while the temperature does not show any definite decay. Moreover, the jet density appears to drop more rapidly than $r_{\rm j}^{-2}$ in the counter-jet. The dissimilarities between the opposite portions of the HH 30 jet may reflect an asymmetry in the accretion/ejection mechanism, as seems to be suggested by the fact that there is not a one-to-one correspondence between the knots in the jet and in the counter-jet (Burrows et al. 1996). Alternatively, the propagation in media of different density stratification may substantially affect the jet physical conditions. New observations at wavelengths less affected by dust extinction would help to clarify this aspect. Either way, the existence of evident asymmetries between the opposite lobes of a stellar jet is a common phenomenon (Hirth et al. 1994).

5. Conclusions

We have investigated the physical structure of the HH 30 jet by applying the spectroscopic diagnostic technique described in Bacciotti & Eislöffel (1999), to a combination of ground-based long-slit spectra and HST narrowband images. The technique allows one to derive from the ratios of the most commonly observed forbidden lines the ionization fraction, the total density and the average excitation temperature in the emission region of the lines considered.

For the central region of the flow (i.e. for the first $5''$ of the jet and for the first $2''$ of the counter-jet from the source) we used HST narrowband images in the [SII] and [OI] lines integrated across the beam (with spatial sampling of $0\farcs1$ along the axis), in conjuction with fits of the electron density and of the [OI]/[NII] ratio derived with $0\farcs6$ spatial sampling by MRBRS90 from a ground-based spectrum. The outermost parts of the flow, i.e. from $5''$ to $12\farcs5$ in the jet and from -$2''$ to -$6''$ in the counter-jet, were investigated using a poorer spatial resolution long-slit spectrum (limited by the pixel size of the detector to $1\farcs8$). In both the HST images and the ground-based spectra the contribution to the emission of the reflection nebula at the base of the flow was carefully subtracted. The outcomes of our analysis can be summarized as follows:

1) Both the jet and the counter-jet are weakly ionized, though $x_{\rm e}$ is higher in the counter-jet. In the jet the ionization fraction rapidly rises from 0.065 at $0\farcs2$ to 0.1 at $0\farcs4$; then slowly *increases* up to 0.140 in two arcseconds, and from $2\farcs4$ to $12\farcs5$ decreases very slowly down to a value of 0.04. The smooth decay of both the ionization fraction and the electron density in the outermost part of the jet is well reproduced by a simple recombination model calculated assuming that the flow channel has a conical shape with *full* opening angle of only 2° beyond $0\farcs7$ from the source. In the few positions examined in the counter-jet, $x_{\rm e}$ rapidly rises from about 0.07 up to 0.25–0.35 at 2–3$''$ from the source.
2) The HH 30 jet is the densest we have examined so far: the total hydrogen density calculated as $n_{\rm H} = n_{\rm e}/x_{\rm e}$ turns out to be at least as high as 10^5 cm^{-3} at the beginning of the main jet, but it decreases to 5 10^4 cm^{-3} within the first arcsecond and then steadily falls to 10^4 cm^{-3} at greater distance. In the counter-jet the total density decreases from about 8 10^4 cm^{-3} to 10^4 cm^{-3} near the source to a few 10^3 cm^{-3} further out.
3) The average excitation temperature is very high within the first arcsecond of the jet, where it rapidly decreases from $\sim$ 2 10^4 K to 10^4 K. Then it decays more slowly to lower values (6000–7000 K) at the end of the visible section. In the counter-jet $T_{\rm e}$ is almost constant at about 1.3–1.5 10^4 K.

These results have several interesting implications:

a) In previous analyses of other jets made at much lower spatial resolution the ionization fraction was generally found to decrease along the flows, on temporal scales consistent with the gas recombination time (see BE99 and references therein). On the contrary, in the HH 30 jet the ionization slowly increases in the first few arcseconds while the temperature rapidly falls from high values. If the ionization is created in the first portion of the flow by a mechanism similar for all jets, then in distant jets, the source of which is still deeply embedded, only the subsequent recombination section would be detected.
b) The shape of the profiles of the ionization fraction and the excitation temperature in the visible section of the jet are reminiscent of the ones predicted for the cooling region of a steady, radiative oblique shock located in the proximity of the source. Only a refined radiative shock model, calculated with input parameters consistent with our results, however, could determine if this picture is correct.
c) We compared the fluxes in the observed lines with the fluxes calculated with the parameters derived by our analysis. In the main jet, which we assumed not to be obscured by dust, the 'effective' diameter of the emitting region, i.e. the diameter of the region at constant $n_{\rm e}$, $x_{\rm e}$ and $T_{\rm e}$, that would produce the observed radiation, is in good agreement with recent measurements of the apparent width of the jet where

resolved (from the observed FWHM, Burrows et al. 1996, Ray et al. 1996). The square of the ratio between the calculated emission-weighted effective radius and the observed radius scatters around an average value of ~ 0.7 along the flow. This implies that *the filling factor is of order unity*, at least in the bright section of the jet. We find no strong evidence for radiative shocks with high compression ratios; there is some evidence, however, for the filling factor to peak at the positions of the knots. The emission-weighted jet radius goes to zero at the source, defining an initial *full* opening angle of about 10°. In contrast, the full opening angle in the collimated portion beyond $0\farcs7$ is only 2°. There are indications, however, that part of the boundary regions of the jet may contain a significant portion of the mass but be too cold to be observable in optical lines.

d) The knots in the HH 30 jet are apparently correlated with local minima of the [SII]/[OI] ratio, which in turn correspond to local temperature peaks. In our data the jet density and the ionization fraction do not show any obvious variation correlated with the emission profile, though we cannot exclude their existence, because of the lower spatial resolution with which $n_{\rm e}$ and $x_{\rm e}$ have been derived. Nevertheless, the resulting small variations in the excitation temperature alone are sufficient to create the knotty emission profile. On the other hand, the absence of density enhancements at the position of the bright knots may indicate the presence of a substantial magnetic field in the body of the jet that inhibits post-shock compression. In any case, the absence of evident bow-shaped features seems to indicate that, at least in the main jet, the bright spots correspond to the location of plasma instabilities rather than internal working surfaces.

e) We calculated the mass loss and momentum transfer rates using the total density and the jet effective radius derived by our analysis, and assuming an average flow speed of 200 km s^{-1}. In the main jet the average mass-loss rate is about 1.7 10^{-9} M$_\odot$ yr^{-1}, and the momentum transfer rate is, in turn, 3.5 10^{-7} M$_\odot$ yr^{-1} km s^{-1}. In the counter-jet, in contrast, $\dot{M}$ ($\dot{P}$) decreases from about 1.8 10^{-9} M$_\odot$ yr^{-1} (3.6 10^{-6} M$_\odot$ yr^{-1} km s^{-1}) close to the source to 9.3 10^{-10} M$_\odot$ yr^{-1} (1.9 10^{-7} M$_\odot$ yr^{-1} km s^{-1}) further out.

f) Our study confirms that the counter-jet is substantially more excited than the jet. Its relative faintness may be due to the fact that it propagates into the parent cloud, and our analysis suggests that it may even be brighter than the jet.

Acknowledgements. FB was supported by an European Space Agency contract at the Dublin Institute for Advanced Studies during the course of this work. We thank the referee, Dr. J. Hatchell, for her valuable comments on a previous version of the manuscript.

References

Allen C., 1973, Astrophysical Quantities. Humanity Press Inc., New Jersey
Bacciotti F., Eislöffel J., 1999, A&A 342, 717 (BE99)
Bacciotti F., Chiuderi C., Pouquet A., 1997, ApJ 478, 594
Bodo G., Massaglia S., Ferrari A., Trussoni E., 1994, A&A 283, 655
Buckle J.V., Hatchell J., Fuller G.A., 1999, A&A in press
Burrows C.J., 1995, WFPC2 Instrument Handbook. STScI, Baltimore
Burrows C.J., Stapelfeldt K.R., Watson A.M., et al., 1996, ApJ 473, 437
Camenzind, M., 1990, Reviews in Modern Astronomy 3, 234
Cohen M., Jones B.F., 1987, ApJ 321, 846
Downes T., Ray T.P., 1999, A&A in press
Eislöffel J., Dougados C., 1997, In: Paresce F. (ed.) Science with the VLT Interferometer. ESO Astrophysics Symposia, Springer, p. 240
Falle S.A.E.G., Raga A.C., 1993, MNRAS 261, 573
Falle S.A.E.G., Raga A.C., 1995, MNRAS 272, 785
Ferreira J., Pelletier G., 1995, A&A 295, 807
Graham J.A., Heyer M.H., 1990, PASP 102, 972
Hardee P.E., Stone J.M., 1997, ApJ 483, 121
Hartigan P., Raymond J., 1993, ApJ 409, 705
Hartigan P., Morse J.A., Raymond J., 1994, ApJ 436, 125
Hartigan P., Edwards S., Gandhour L., 1995a, ApJ 452, 736
Hartigan P., Morse J.A., Raymond J., 1995b, ApJ 444, 943
Hirth G.A., Mundt R., Solf J., Ray T.P., 1994, ApJ 427, L99
Hirth G.A., Mundt R., Solf J., 1997, A&AS 126, 437
Kenyon S.J., Dobrzycka D., Hartmann L., 1994, AJ 108, 1872
Lavalley C., Cabrit S., Dougados C., Ferruit P., Bacon R., 1997, A&A 327, 671
López R., Raga A.C., Riera A., Anglada G., Estalella R., 1995, MNRAS 274, L19
Mellema G., Frank A., 1997, MNRAS 292, 795
Micono M., Massaglia S., Bodo G., Rossi P., Ferrari A., 1998, A&A 333, 989
Mundt R., Fried J.W., 1983, ApJ 274, L83
Mundt R., Ray T.P., Bührke T., Raga A.C., Solf J., 1990, A&A 232, 37 (MRBRS90)
Ouyed R., Pudritz R.E., 1993, ApJ 418, 255
Ouyed R., Pudritz R.E., 1997, ApJ 482, 712
Raga A.C., Cantò J., 1998, Rev. Mex. Astron. Astrofis. 34, 73
Raga A.C., López R., Riera A., Estalella R., Anglada G., 1997, Rev. Mex. Astron. Astrofis. 33, 127
Ray T.P., 1996, In: Tsinganos K. (ed.) The NATO ASI on: Solar and Astrophysical MHD Flows. Heraklion Crete, Kluwer Academic Publishers, 539
Ray T.P., Mundt R., Dyson J.E., Falle S.A.E.G., Raga A.C., 1996, ApJ 468, L103
Safier P.N., 1993a, ApJ 408,115
Safier P.N., 1993b, ApJ 408,148
Shu F.H., Najita J., Ostriker E., Shang H., 1995, ApJ 455, L155
Stone J.M., Norman M.L., 1993, ApJ 413, 210
Stone J.M., Xu J., Hardee P.E., 1997, ApJ 483, 136